Supplementary Material

1 Supplementary Methods

1.1 Clinical data of each patient in the study

Supplementary Table 1. Clinical data of each patient in the study.

[a]CC = Cleveland Clinic, KUMC = University of Kansas Medical Center, JHU = Johns Hopkins Hospital, Miami = University of Miami Hospital, NIH = National Institutes of Health, UPMC = University of Pittsburgh Medical Center

[b]S = Success, F = Failure

[c]R = Right, L = Left

[d]F = Female, M = Male

[e]MTLE = Mesial-Temporal Lobe Epilepsy, NMTLE = Non-Mesial-Temporal Lobe Epilepsy

Patient ID	Center[a]	Engel	ILAE	Outcome[b]	Race	Age	Hand[c]	Gender[d]	Surgery Type	# Channels	EZ Channels	Treated Channels	MTLE/NMTLE[e]	Epilepsy Type	MRI Findings
la02	CC	1	1	S	0	19	R	F	ablation	60	L'2-4	L'1-5	NMTLE	Focal	Normal
la03	CC	2	2	F	0	37	R	M	ablation	102	L7, W12-14, X6-10, O14-16, F10-12	L5-9	NMTLE	Focal	Normal
la04	CC	2	4	F	0	32	R	M	ablation	76	L'4, G'1-15	L'2-6, G'1-3	NMTLE	Focal	Normal
la05	CC	2	2	F	0	29	R	M	ablation	138	D'1-2, U'3-5, D1-2, S'7-11, S7-11, T'1-3, T1-3	T'1-4, D'1-4	NMTLE	Focal	Normal
la06	CC	2	3	F	0	37	R	F	ablation	75	Q'3-4, R'3-4	Q'1-6, R'1-6	NMTLE	Focal	Normal
la08	CC	3	4	F	0	24	R	F	ablation	84	Q1-3	Q1-4	NMTLE	Focal	Normal
la09	CC	2	4	F	0	34	R	F	ablation	155	X'1-4, U'1-2, P'1-2	P'1-4	NMTLE	Focal	Normal
la10	CC	2	5	F	0	20	R	M	ablation	118	S1-2, R2-3	S1-4, R1-5	NMTLE	Focal	Normal
la11	CC	2	4	F	0	22	R	M	ablation	134	D6, Z10	D4-8, Z8-12	NMTLE	Focal	Normal
la13	CC	1	2	S	0	43	R	M	ablation	50	Y13-14	Y11-16	NMTLE	Focal	Normal
la15	CC	4	5	F	0	22	R	M	ablation	136	R1-3	R1-5	NMTLE	Multi-Focal	Normal
la16	CC	4	5	F	0	37	R	M	ablation	125	Y1-2, M'1-2, X'1-2, Q7-8	Q7-8	NMTLE	Multi-Focal	Normal
la21	CC	1	1	S	0	40	R	M	ablation	115	J6-9, X5-8, Y11-Y16	J6-9, X5-8	NMTLE	Focal	Abnormal
la22	CC	2	4	F	2	44	R	F	ablation	126	P3-4	P3-4	NMTLE	Focal	Normal
la23	CC	1	1	S	0	28	L	F	ablation	119	L1-2, O1-2, V1-2, V4-5, C1-4, U1-6, F6-7, I1-10	L1-2, O1-2, V1-2	NMTLE	Focal	Abnormal
la24	CC	2	3	F	0	19	R	F	ablation	133	C'6-7, L'6-7, O'6-7	C'6-7, L'6-7, O'6-7	NMTLE	Focal	Abnormal
nl01	CC	3	2	F	0	24	R	F	resection	153	M'8-12	M'8-10	NMTLE	Focal	Normal
nl04	CC	1	2	S	N/A	16	L	M	resection	97	R'1-5, Q'2-3, R6-7, Q1-2	R'1-6, H'5-10, S'6-10	NMTLE	Focal	Normal
nl05	CC	1	2	S	0	23	L	M	resection	94	M'7-9, W'2-3, W'9-12, Y'1-7, Y'10-13, Z'1-3, Z'9	W'1-12, Y'1-14, Z'1-9	NMTLE	Focal	Normal
nl07	CC	1	1	S	0	37	R	F	resection	56	R5-7, Q7-9, R'5-7, M2-5	R5-10	NMTLE	Focal	Normal
nl08	CC	1	1	S	0	16	R	F	resection	91	I'1-4, A'1-4, B'1-4, C'1-4, E'1-4	A'1-14, E'1-14, I'1-10	MTLE	Focal	Normal
nl12	CC	4	5	F	0	16	R	M	resection	135	A2-14, I1-8, T3-9	A2-14, I1-8, T3-9	NMTLE	Focal	Normal
nl13	CC	1	1	S	0	65	R	F	resection	68	B'1-4, C'1-3, T'1-9	B'1-4, C'1-3, T'1-10	NMTLE	Focal	Normal
nl14	CC	2	4	F	0	43	R	M	resection	123	X1-3, X5-6, X9-14, E4-5	B1-14, E1-12, F1-11, X1-16	NMTLE	Focal	Normal
nl15	CC	1	2	S	0	31	R	F	resection	54	B1-3, A1-3	A1-10, B1-10, I1-6, E1-7	MTLE	Focal	Normal
nl16	CC	1	1	S	0	25	R	F	resection	71	B'8-9, C'9-10, E'7-8, I'1-16	A'1-14, B'1-3, E'1-10, I'1-9	NMTLE	Focal	Normal
nl18	CC	1	1	S	0	18	R	F	resection	99	A1-2, B1-2, C1-4	A1-14, I1-8, T1-8, B1-14, C1-14	NMTLE	Focal	Normal
nl19	CC	3	3	F	1	25	L	M	resection	99	A1-2	A1-12, I1-9, T1-8	NMTLE	Focal	Normal
nl20	CC	1	1	S	0	58	R	F	resection	58	A'1-10, I'1-7, T'4-6, B'1-10	A'1-10, I'1-7, T'4-6, B'1-10	MTLE	Focal	Normal
pt1	KUMC	1	2	S	N/A	24	N/A	F	resection	62	RST5-8	RST5-8	NMTLE	Focal	Abnormal
pt3	KUMC	1	2	S	N/A	35	N/A	F	resection	83	RHH1-2	RTP1-6, RHH1-8	MTLE	Multi-Focal	Abnormal
pt4	KUMC	2	4	F	N/A	31	N/A	F	resection	125	LAC1-2, LMC1	LMC1-2	NMTLE	Focal	Normal
pt6	KUMC	3	4	F	N/A	57	N/A	M	ablation	45	LHB1-3, LHH1-3	LHH1-3, LHB1-3	MTLE	Focal	Normal
pt8	KUMC	2	3	F	N/A	27	N/A	F	resection	128	RHH1-7	RHH1-14	MTLE	Focal	Normal
pt10	KUMC	1	1	S	N/A	35	N/A	F	resection	94	RHB1-4	RAM1-6, RHB1-5	MTLE	Focal	Normal
pt11	KUMC	2	1	F	N/A	68	N/A	M	resection	49	LSTG2, LSTGC1-2, LAM1-4, LHH1-3	LAM1-14, LHH1-14, LENC1-10	MTLE	Multi-Focal	Normal
pt12	KUMC	2	3	F	N/A	22	N/A	M	resection	59	OF8-9	OF7-9, LA3-6, MA1-6, MB1-6	NMTLE	Focal	Abnormal
pt13	KUMC	1	1	S	N/A	58	N/A	F	resection	76	RHH5-6	RHH1-8, RHB1-8, RAM1-8	MTLE	Focal	Normal
PY18N002	JHU	2	2	F	N/A	62	N/A	M	resection	95	RHD1-2, RAD1-2, LMFD1-2, ßLOFD1-2	RHD1-2, RAD1-2	MTLE	Multi-Focal	Abnormal
PY18N013	JHU	1	1	S	N/A	24	N/A	F	resection	126	LTP1-4, LSTA1-2, LMTA2	LTP1-4, LSTA1-2, LMTA2, L Amygdala	MTLE	Focal	Abnormal
PY18N015	JHU	1	1	S	N/A	N/A	N/A	F	resection	76	LOF1, LA1-3, LH1-3	LOF1-14	NMTLE	Focal	Abnormal
PY19N015	JHU	3	4	F	N/A	23	N/A	M	RNS	87	LBT1-3, LHP1-2, LA1-2, LHA1-3	N/A	MTLE	Focal	Abnormal
PY19N023	JHU	1	1	S	N/A	32	N/A	M	resection	87	RA1-2, RAH1-2, RPH1-2, RMI3-5, RMM5-6	N/A	MTLE	Focal	Abnormal
002	Miami	3	N/A	F	N/A	36	R	F	RNS	123	DYS5-8	N/A	MTLE	Multi-Focal	Abnormal
003	Miami	3	N/A	F	N/A	21	L	M	RNS	97	LIS1-6	N/A	NMTLE	Multi-Focal	Abnormal
004	Miami	4	N/A	F	N/A	52	L	M	RNS	40	H1-2	N/A	MTLE	Focal	Normal
006	Miami	1	N/A	S	N/A	49	R	M	RNS	39	LAI1-3, LSF3-4, LAC5-7, LMF5-7	N/A	NMTLE	Focal	Normal
009	Miami	3	N/A	F	N/A	48	R	M	RNS	28	RTL1-3, RAT1-3	N/A	MTLE	Multi-Focal	Normal
011	Miami	4	N/A	F	N/A	24	R	F	RNS	80	ROF6-12	N/A	NMTLE	Focal	Normal
013	Miami	2	N/A	F	N/A	25	R	M	RNS	36	RAI9-12	N/A	MTLE	Focal	Normal
015	Miami	2	N/A	F	N/A	27	R/L	M	RNS	57	LFP1-6	N/A	NMTLE	Multi-Focal	Normal
nih2	NIH	1	1	S	1	31	R	M	resection	89	RAID1-4, RIPI1-2, RPHD1-3	RATO1-10, RPTO1-10, RPHD1-4, RIPI1-2, RAID1-2	NMTLE	Multi-Focal	Normal
nih3	NIH	1	1	S	0	36	R	F	resection	89	LAD2-6, LAHD4-5, LAHD13-14, LAD10-12, LOF9-10, LPFC1-2	LAD1-10	NMTLE	Multi-Focal	Normal
nih4	NIH	1	1	S	0	39	R	M	resection	94	RSLP8-9, RILP7, RSMP3	RSLP5-10, RILP5-10	NMTLE	Multi-Focal	Abnormal
nih5	NIH	1	1	S	0	41	R	M	resection	97	SAF6-7, IEPF3, SPF8-12, IPF9-11, SMF7-8, IEAF9-10	IEAF9-10, IAF8-11, SMF6-9, SPF7-8, SAF6-9	NMTLE	Focal	Normal
nih7	NIH	3	4	F	0	46	R	M	resection	106	LPH1-3, LAH1-5	LAH1-6, LPH1-4, LALT6	MTLE	Multi-Focal	Abnormal
nih8	NIH	2	4	F	0	37	R	M	resection	153	LPT1-6	LPT1-16	MTLE	Focal	Normal
nih9	NIH	3	4	F	0	16	L	F	resection	119	AID4-8	PLF1-3, ALP1-4, PLP1-6	NMTLE	Focal	Abnormal
nih10	NIH	2	3	F	0	25	R	M	resection	83	LAID6-8	LAID2-10	NMTLE	Focal	Normal
nih11	NIH	2	3	F	0	27	R	M	resection	112	LSA5-8, MPF6-12, LIA1-6	MAF4-10, LSA4-8, LMA4-8, LIA7-8	NMTLE	Focal	Abnormal
upmc1	UPMC	1	1	S	N/A	44	R	M	resection	131	B1-4, C3-5, A1-3	A1-16, B1-16, C1-5, T1-16, I1-16, E1-16	MTLE	Focal	Normal
upmc2	UPMC	1	1	S	N/A	46	R	F	resection	110	A'1-4, B'1-6, C'1-6, E'1-6	A'1-16, B'1-16, C'1-5, T'1-16, I'-16, E'1-16	MTLE	Focal	Abnormal
upmc3	UPMC	2	3	F	N/A	24	R	M	resection	122	A1-5, B1-5, E1-5	A1-5, B1-5, E1-5, I1-5	MTLE	Focal	Normal
upmc5	UPMC	4	5	F	N/A	46	R	F	resection	122	T'3-6, E'1-5, F'2-4	J'10-15, I'1-16, A'1-16, E'1-16, B'1-16, T'3-8, C'1-4, F'1-10	NMTLE	Focal	Normal
upmc6	UPMC	1	1	S	N/A	23	R	M	resection	92	B1-4, A1-4, C1-4	J10-15, I1-16, A1-16, E1-16, B1-16, T3-8, C1-4	MTLE	Focal	Normal

1.2 Example of reconstructed versus actual iEEG signals
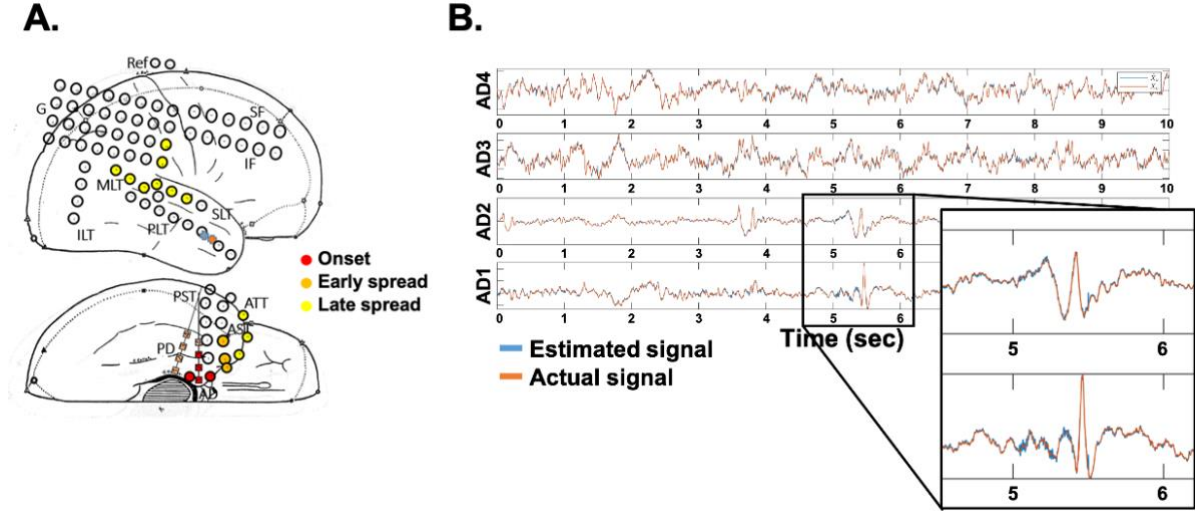
Supplementary Figure 1. A. ECoG implantation of patient. B) 10 second snapshot of actual (orange) versus simulated (blue) signals of four iEEG channels from one depth electrode. All four channels belong to the clinically annotated EZ. Interictal spikes, present in two signals (AD1-2), are accurately captured by the network model.

1.3 Details of source-sink analysis to localize the EZ

For each patient, the interictal SEEG recording was split into 500-msec non-overlapping windows and the dynamical network models (DNMs) were estimated in every window w of the data to obtain a sequence of $\boldsymbol{A}$ matrices over time, $\boldsymbol{A}_w, w \epsilon [1, 2, ..., T]$, where T is the number of windows. In $\boldsymbol{A}_w$ (Fig. 2C), row i represents the amount of influence SEEG channel i receives from the rest of the network in window w, and column j represents how the activity of channel j influences the activity of all other channels in the network.

1.3.1 Identifying top sources and sinks in the interictal SEEG network

To identify the top sources and sinks in each patient's DNM, we quantified each channel's source-sink characteristics by computing the amount of influence to and from the channel as follows. The total influence channel i received from the rest of the network in window w was defined as the sum of the absolute values across its row in $\boldsymbol{A}_w$ or in other words, the 1-norm of its row. Similarly, we defined the total influence from channel i to the rest of the network as the 1-norm of its column in $\boldsymbol{A}_w$. Then, we placed each channel in the 2D source-sink space (SS-space, Fig. 2D) by ranking the row and the column norms of all channels against each other (where rank $\frac{1}{N}$ indicates the smallest 1-norm and rank 1 is the largest 1-norm) to obtain each channel's row rank (rr) and column rank (cr). When drawn in the 2D SS-space (Fig.

2D), sources are channels located at the top left (blue circles), whereas sinks (pink circles) are located at the bottom right.

1.3.2 Computing source-sink metrics: A 4-node example

Consider the 4-node network example in Supplementary Fig. 2. Node 3 is a source node because it is highly influential on all nodes, specifically nodes 2 and 4, in the network. In contrast, nodes 2 and 4 are sink nodes because they are highly influenced by other nodes, specifically node 3, and they do not have a high influence on other nodes in the network. This is reflected in the rows and columns of the A matrix of the DNM. A sink node will have nearly all zeros in its column vector in A (blue in Supplementary Fig. 2B) because it does not impact the future activity of its neighbors; but its row vector will all be close to one (red in Supplementary Fig. 2B) because it is highly influenced by all the other nodes. Source nodes have the opposite properties in the A matrix. Their columns are red and rows are blue (see column and row 3 in Supplementary Fig. 2B). As described above, all nodes can be quantified as more of a sink or more of a source by computing the amount of influence to and from the node based on the sum of the absolute values (the 1-norm) across its row and column in A, respectively, and ranking them against each other (where rank 1/N indicates smallest 1-norm (i.e., low influence), and rank 1 is the largest 1-norm (high influence) for a network with N nodes). We then place the nodes in the 2D-Space shown in Supplementary Fig. 2C, where sources are located at the top left (high column rank, low row rank), and sinks are located at the bottom right (low column rank, high row rank).

Consider node 2, which is a sink in the network and thus is located near the bottom right corner in the source-sink 2D-Space (Supplementary Fig. 2C). More specifically, the node's row rank is $rr_2 = 1$ and its column rank is $cr_2 = \frac{1}{4}$. We start by computing the node's sink index to quantify how close it is to the ideal sink (pink star in Supplementary Fig. 2C, with $rr = 1$ and $cr = \frac{1}{4}$). Using (2) in the main manuscript we get:

$$sink_2 = \sqrt{2} - \left\|\left(1,\frac{1}{4}\right) - \left(1,\frac{1}{4}\right)\right\| = \sqrt{2}$$

Similarly, we compute node 2's source index using (3):

$$source_2 = \sqrt{2} - \left\|\left(1,\frac{1}{4}\right) - \left(\frac{1}{4},1\right)\right\| = \frac{\sqrt{2}}{4}$$

Now, we can compute the node's source influence using (4) to quantify how much it is influenced by the top sources in the network. We do this by computing the sum across the second row of the A matrix, weighted by each node's source index:

$$infl_2 = 0.7 * 0.75 + 1 * 0.25 + 0.9 * 1 + 0.8 * 0.5 = 2.075$$

Lastly, we compute node 2's sink connectivity index to quantify how much it is influenced by the sinks in the network. Similar to the source influence index, we are interested in the strength of connections from other sinks *to* node 2, and thus we use the second *row* of the A matrix, but now we weigh the sum by each node's sink index. We compute the sink connectivity using (5) as:

$$conn_2 = 0.7 * 0.5 + 1 * 1 + 0.9 * 0.25 + 0.8 * 0.75 = 2.175$$

Finally, each metric is normalized by its maximum value across the network (which in this example happens to be node 2's values for all metrics) to obtain:

$$sink_2 = \frac{\sqrt{2}}{\sqrt{2}} = \mathbf{1}$$

$$infl_2 = \frac{2.075}{2.075} = \mathbf{1}$$

$$conn_2 = \frac{2.175}{2.175} = \mathbf{1}$$
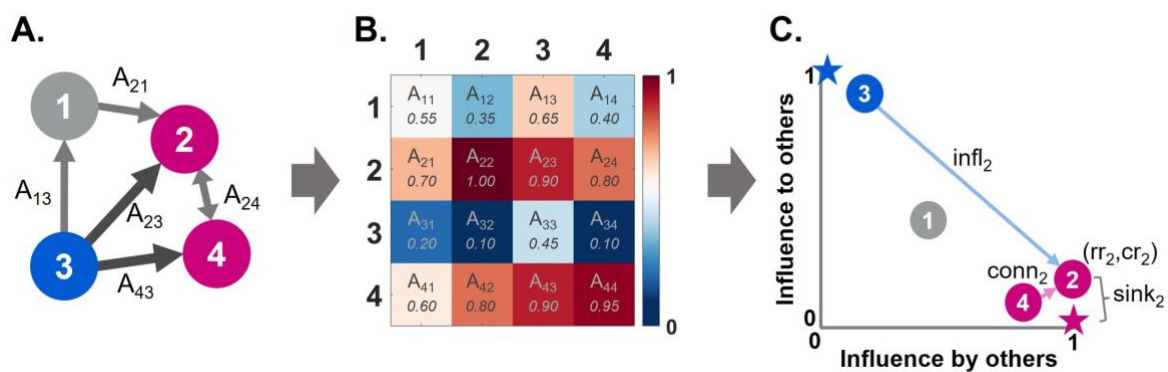
Supplementary Figure 2. A. A 4 node network example. B. Corresponding mean A matrix. Example values are given in each cell of the matrix. C. 2D source-sink representation of the network with sink index (sink$_2$), source influence (source$_2$) and sink connectivity (conn$_2$) of node 2 labeled. Sources (blue) are located at the top left whereas sinks (pink) are located at the bottom right. Blue star = ideal source, pink star = ideal sink.

1.3.3 Computing average source-sink metrics

Unlike seizure activity, interictal activity is relatively stable, with little deviation from a baseline value over time. As a result, there is little variation in the sequence of $\boldsymbol{A}_w$ matrices and consequently the source-sink behavior of individual channels across windows during interictal periods. Thus, we also defined a single, constant $\boldsymbol{A}$ matrix to represent each patient's interictal DNM as:

$$\boldsymbol{A} = \frac{1}{T} \sum_{w=1}^{T} abs(\boldsymbol{A}_w) \tag{1}$$

Finally, in addition to computing the source-sink metrics (SSMs) across windows using $\boldsymbol{A}_w$ we also computed a set of constant SSMs for each patient using $\boldsymbol{A}$ in (1).

1.4 Quantifying temporal stability of source-sink metrics

Because of the relative stability of the interictal activity over time, we expect SSMs to be consistent and independent of the timing or duration of the interictal snapshot used for each patient. To verify that the channels reported to clinicians with largest SSMs were consistent over time, we quantified the temporal stability of the source-sink metrics for each patient as follows. Let A_m be the set of iEEG channels with the highest 10% of values for each constant, average, metric $m = \{sink, infl, conn, ss\}$, computed from $\boldsymbol{A}$ averaged across the entire interictal recording (eq. 1), and let B_m^w be the set of the top 10% of channels with highest values for each metric m computed from the average $\boldsymbol{A}$ of a smaller window $w \epsilon \{1, \dots, W\}$ of size ws, where W is the number of non-overlapping windows of size ws across the patient's interictal recording. Finally, let C_m be a set of randomly selected channels of the same size as A_m and B_m^{ws}. Then, in each window w, we computed the percentage of channels in B_m^{ws} that were also A_m, i.e.

$$AB_m^{ws} = \frac{|A_m \cap B_m^{ws}|}{|A_m|} * 100 \tag{2}$$

Similarly, we computed CB_m^{ws} as the percentage of channels in B_m^{ws} that were also in C_m. Finally, we computed the average percentage of channels captured across all windows for each metric to obtain a distribution of AB_m^{ws} and CB_m^{ws} across patients, and compared to the average percentage expected for randomly selected channels as described below. We chose this analysis to quantify whether the results presented back to clinicians, i.e., the channels with the largest SSMs, remained consistent across time.

1.4.1 Statistical Analysis

We repeated the analysis for five different window sizes, $ws = \{1, 2, 3, 5, 10\}$ minutes. Specifically, for each ws, we split each patient's recording into non-overlapping windows of length ws and computed the percentage iEEG channels with 10% highest SSM values captured on average across all windows as well as the average percentage of top channels that were captured by chance (Fig. 4). CB_m was computed for 10 different sequences of randomly sampled channels in each window. Then, we compared AB_m^{ws} and CB_m^{ws} for each m and each ws using a paired two-sample t-test with the null hypothesis that the two distributions have equal means and the alternate hypothesis that the means are different. A p-value ≤ 0.05 was considered to be statistically significant.

1.5 Details on predicting surgical outcomes using source-sink metrics

To evaluate the SSMs as interictal iEEG markers of the EZ, we tested their efficacy in predicting surgical outcomes following the same procedure as Li et al.[1] (Supplementary Fig. 3) and compared performance against that of clinicians as well as HFOs, the most common interictal iEEG marker of the EZ.

Specifically, we modeled the probability of a successful surgical outcome, p_s, as a function of the three SSMs (sink index, source influence and sink connectivity) using a sparse oblique
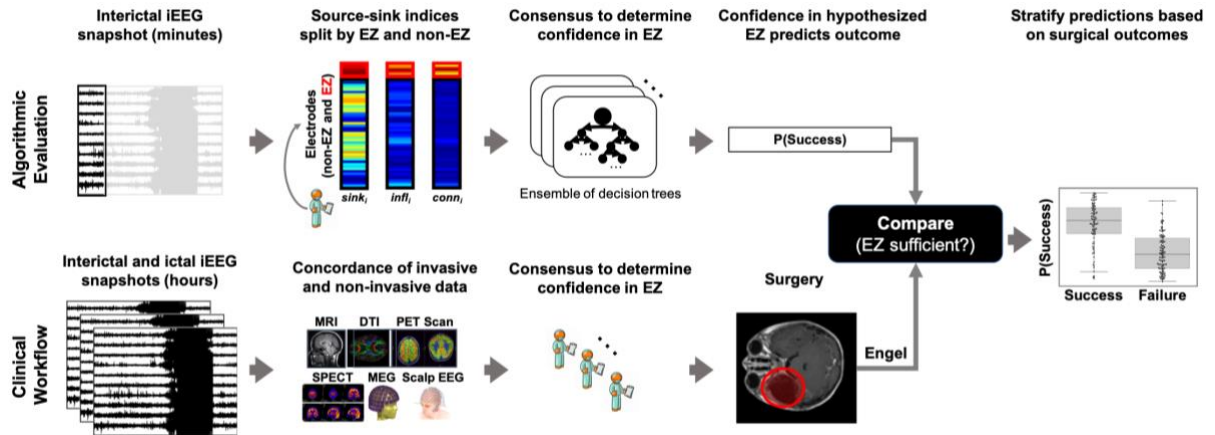
Supplementary Figure 3. Schematic of the experimental design for predicting surgical outcomes. Top: From just minutes of iEEG data from each patient, we compute a set of constant, average, source-sink metrics for each iEEG channel. We summarize the metrics by computing the mean and s.d. of each metric across i) EZ channels and ii) non-EZ channels and use as features in the RF classifier to compute a probability of success p_s for the patient. Finally, we apply a threshold to p_s to predict surgical outcome and compare to the actual outcome of the patient. Bottom: A simplified diagram of the clinical workflow from pre-surgical evaluation to surgical treatment of MRE patients. The clinical team visually inspects hours of interictal and ictal iEEG data, in addition to various non-invasive data to come to a consensus on which electrodes are recording from the EZ. Lastly, surgery is planned to remove the EZ.

random forest (RF) classifier, known as SPORF.[2,3] We computed the distribution of constant feature values in two sets of channels: i) the CA-EZ and ii) all other channels not labeled as CA-EZ (CA-NEZ). In general, the prediction of surgical outcomes using any feature (e.g., SSM or HFO rate) conditioned on the clinically annotated EZ enables us to evaluate the overall value of the feature as a potential EZ marker. Feature distributions of each set were summarized with the mean and standard deviation, resulting in 12 possible features presented to the RF classifier. Next, we performed a tenfold nested leave-patient-out cross-validation (CV), considering a set of hyperparameters where 70% of the data was used for training the models, and the remaining 30% of the data was held out for test evaluation for each cross-validation iteration. We performed a total of 10 iterations (i.e., tenfold CV). The cross-validation split the data by patients in a "leave patients out" manner (i.e., 70% of the data for 65 patients means that 46 randomly chosen patient recordings were used to train the models in each CV iteration). Finally, we performed statistical analysis (described in the main manuscript) on the final classification performance to determine the most robust feature representation.

1.6 HFO detection

HFOs were detected using two different detectors: a) The Hilbert detector developed by Crépon et al.[4] and b) the root-mean-square (RMS) detector by Staba et al.[5] For each patient, the entire available interictal snapshot was used for HFO detection. HFO events were computed for each channel independently, and rates were recorded as the number of events per minute. We note that we did not perform parameter optimization for this dataset when implementing the detectors though optimization has been shown to impact performance.[6–8] Further, although we chose to test two different detectors for comparison, studies have shown that once detector parameters are properly optimized, the choice of detection scheme is not critical as performance is generally comparable.[7]

1.6.1 The Hilbert detector

The Hilbert detector was ran using the RIPPLELAB toolbox[9], a MATLAB open-source application developed by Navarrete et al. to facilitate the analysis of HFOs. First, iEEG signals were referenced using a monopolar montage and then bandpass filtered between 80-500 Hz (for data sampled at 1000 Hz or above, 80-250 Hz for data sampled at 500 or 512 Hz) before computing the signal envelope using a Hilbert transform. Next, its local maxima exceeding 5 standard deviations of the envelope over the whole signal and with a minimal time length of 10 mseconds were automatically detected and labeled as HFOs.

1.6.2 The RMS detector

First, the iEEG signals were re-referenced to a bipolar montage and artifactual segments were removed using an automated extreme value detector.[10,11] Neural data in each channel were then bandpass filtered between 100-450 Hz (for data sampled at 1000 Hz or above, 100-200 Hz for data sampled between 500 and 1000 Hz) with a finite impulse response filter (passband frequency range of 100-450 Hz, or 100-200 Hz with a stopband of 10Hz). Signals were filtered both forwards and backwards in time to avoid phase distortion. The root-mean-square of each point was computed, and segments of data in which the RMS value exceeded 5 standard deviations above the mean for at least 6 mseconds were recorded. After this initial detection, segments were defined as HFO events if the amplitude of at least 6 rectified peaks (three full oscillations) exceeded a threshold of 3 standard deviations above the mean of the rectified signal.

1.7 Quantifying CA-EZ and SSM correspondence

To quantify the overlap between the CA-EZ and regions with high SSMs, we used them to predict the likelihood of a sEEG channel (region) being in the EZ or not. Specifically, we modeled the probability of being in the EZ (p_{EZ}) as a function of the three SSMs using a logistic regression (LR) model as follows:

$$\log\left(\frac{p_{EZ}}{1 - p_{EZ}}\right) = \beta_0 + \beta_1 SSI$$

where SSI is the source-sink index, defined as the product of the three SSMs.

Since no ground truth of the true EZ exists, the LR model was trained, validated and tested on seizure-free patients only, as we can assume that the EZ was accurately localized in these patients. Out of the 28 seizure-free patients in our dataset, 26 had an accurately localized EZ as determined by clinicians. For those patients, the LR model was validated using a 10-fold cross-validation (CV) by creating ten random splits of the dataset into training and test sets. In each such split, 70% of the sEEG channels were assigned to the training set and the remaining 30% were used for testing, while at the same time ensuring a balanced number of EZ and non-EZ channels by randomly sampling the EZ channels with replacement. The model was fit to the training data and validated on the test set by applying a varying threshold to the model's output and computing a receiver operating characteristic (ROC) curve which plots true positive rates against false positive rates for various threshold values. In addition to the AUC, we used four metrics to measure model performance:

a) prediction accuracy, b) precision, c) sensitivity, and d) specificity. We report results of the ten CV iterations (mean $\pm$ standard deviation) below.
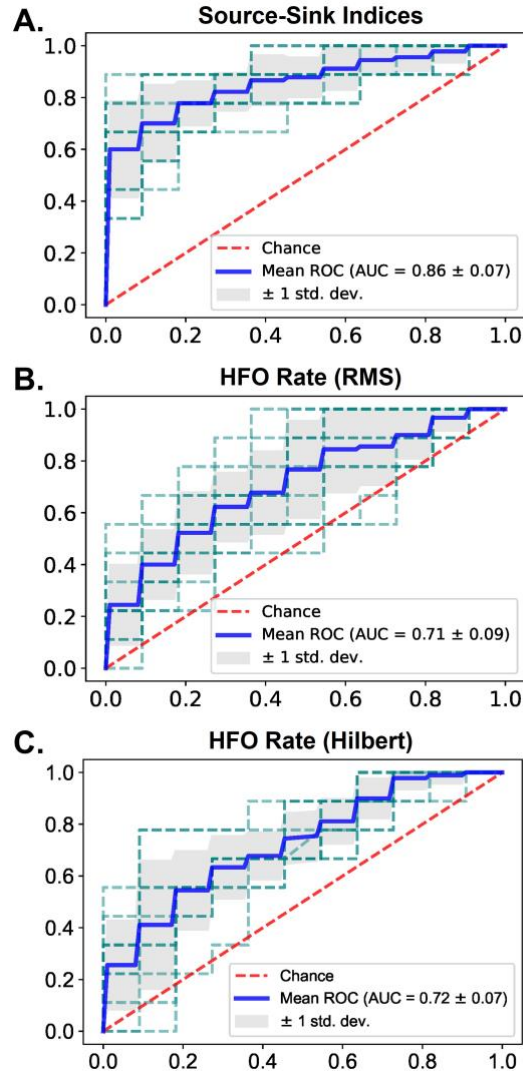
2 Supplemental Results

2.1 Statistical analysis of source-sink metric distributions

Supplementary Table 2. Comparison of source-sink metric distributions in EZ versus non-EZ channels.

	P-value	
	Success patients	**Failure patients**
Sink index	1.1997×10^{-6}	0.0076
Source influence	1.6217×10^{-7}	0.3331
Sink connectivity	1.3070×10^{-7}	0.0771

2.2 Predicting surgical outcomes

2.2.1 Test set ROC curves

Supplementary Figure 4. Test set ROC curves. A. ROC curves for the source-sink model. Blue line shows the mean ROC across the ten CV folds and the shaded gray area represents one standard deviation. The resulting ROC of each CV fold is shown with a dashed green line. B. ROC for the HFO-RMS model. The mean AUC of the RMS model is significantly lower than the mean AUC of the source-sink model. C. ROC for the HFO-Hilbert model. The mean AUC of the Hilbert model is significantly lower than the mean AUC of the source-sink model. However, the mean AUC is not significantly different from the AUC of the RMS model.

2.2.2 Outcome prediction using HFOs detected by the RMS detector

Supplementary Fig. 5 shows p_s distributions across all CV-folds, using the HFO model. The dots are color-coded based on each patient's surgical outcome. A decision threshold of $\alpha = 0.5$ was applied to the estimated probabilities (p_s) to predict each patient's outcome. Using the
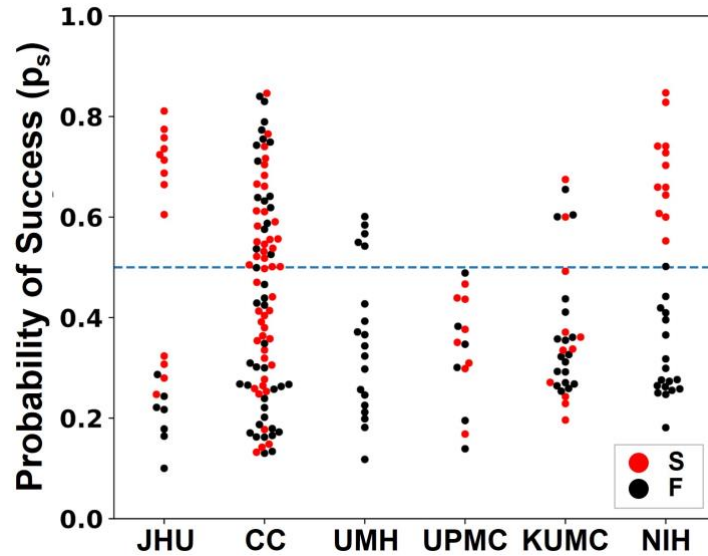
Supplementary Figure 5. Predicted probability of success (p_s) by the HFO-RMS model across all ten CV folds. Each dot represents one patient in one fold and dots are color-coded by surgical outcome. S = success, F = failure. The dashed blue line represents the decision threshold applied to p_s to predict outcomes. There is not a clear separation between the success and failure patients, with both groups having p_s above and below the decision threshold, resulting in lower prediction accuracy compared to the source-sink model.

HFO rate did not yield a clear separation between success and failure patients. In fact, the separation between the p_s distributions of success versus failure patients is greater for the source-sink model (Supplementary Fig. 6A) compared to the HFO model, and consequently so is the model's ability to discriminate between the two outcome possibilities. In fact, we compared the performance of the two models with a contingency table (confusion matrix) and observed that the SSM model was statistically better with a p-value of $p = 0.007$. When further broken down by Engel class (Supplementary Fig. 6B) or ILAE score (Supplementary Fig. 6C), we observed a decreasing trend of p_s as the outcome score (and thus also the severity of post-
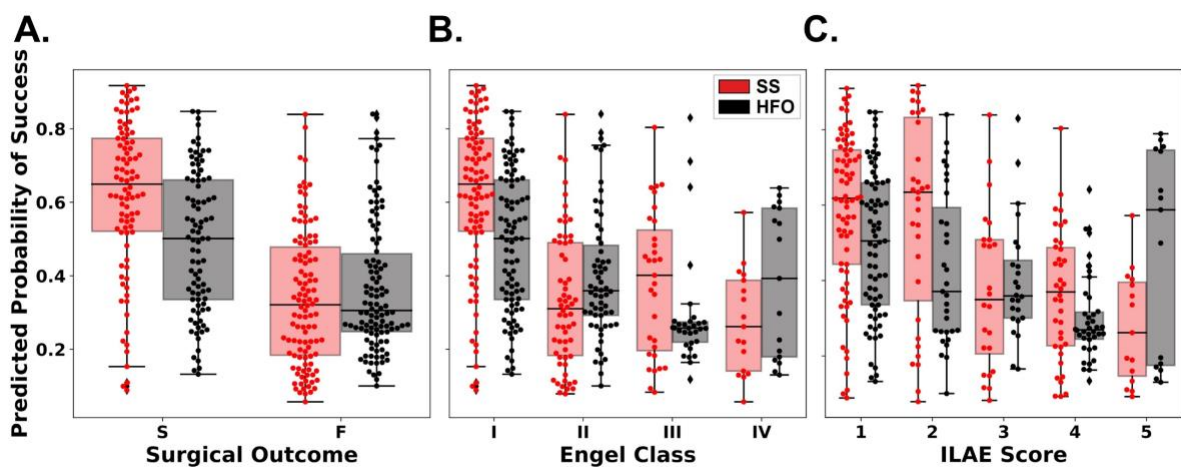
Supplementary Figure 6. Performance comparison of the SSMs (red) to HFO rate (black). Boxes show distributions of each metric across the 10 CV folds. The asterisks indicate a statistically significant difference.

operative seizure outcome) increased using the SSMs. In contrast we did not see this clear separation of p_s values using the HFO model, which had a much greater overlap between classes.

Finally, Supplementary Fig. 7 compares the performance of the SSMs and RMS-HFOs in predicting surgical outcomes. The SSMs outperformed HFO rate with significantly higher AUC, accuracy, average precision and sensitivity ($p_{AUC} = 0.0096$, $p_{accuracy} = 0.0442$, $p_{precision} = 0.0023$ and $p_{sensitivity} = 2.03 \times 10^{-4}$). Although the SSMs had a higher specificity on average, both models performed similarly ($p_{specificity} = 0.7846$). The SSMs had an AUC of 0.86 ± 0.07 compared to an AUC of 0.71 ± 0.10 using HFO rate. The source-sink model also outperformed HFOs in terms of average precision, which weighs the predictive power in terms of the total number of patients, with an average precision of 0.88 ± 0.06 compared to 0.71 ± 0.09 for the HFO rate. Using the SSMs, a threshold of $\alpha = 0.5$ applied to p_s for each subject rendered a test-set accuracy of $79.0 \pm 9.1\%$, compared to a considerably lower accuracy of $65.5 \pm 11.4\%$ using HFOs and an even lower clinical success rate of 43% in this dataset. The biggest performance difference between the two models was in terms of sensitivity (true positive rate) where the SSMs outperformed HFO rate by more than 50%, with a sensitivity of 0.78 ± 0.09. However, both models performed similarly in predicting failed outcomes correctly, where the source-sink model had a slightly higher specificity of 0.80 ± 0.16 compared to 0.77 ± 0.20 for the HFOs.
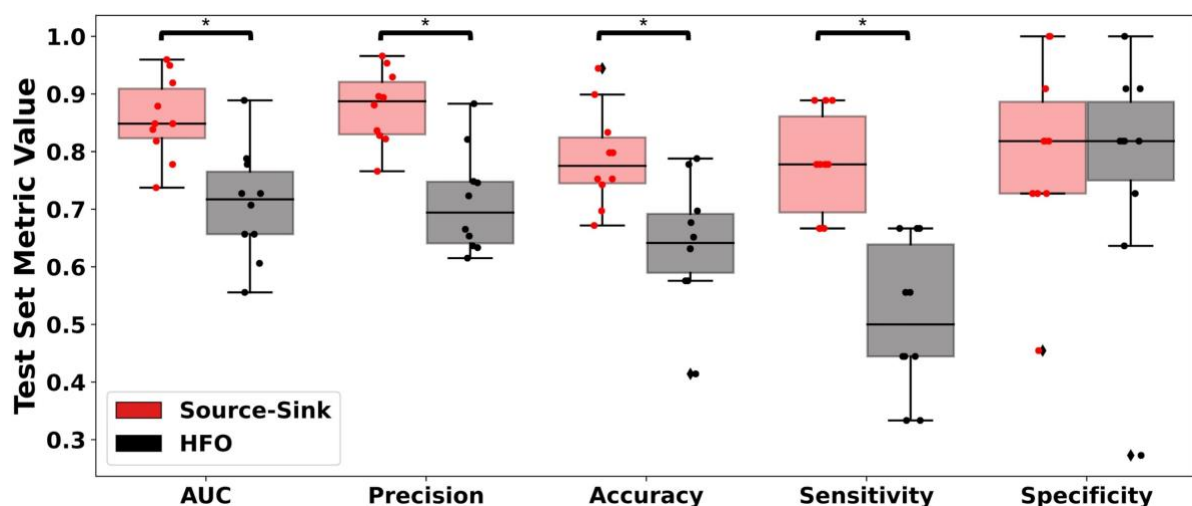

Supplementary Figure 7. Performance comparison of the SSMs (red) to HFO rate (black). Boxes show distributions of each metric across the 10 CV folds. The asterisks indicate a statistically significant difference.

## 2.3 Generalizability of the source-sink metrics

Although lesional patients frequently have better localizable EZ and thus tend to have higher chances of successful outcomes, we saw no correlation to the predicted probability of success nor clinical correspondence in our models (see Supplementary Figs. 8A and 12A). Similarly, our tool was also agnostic to whether patients had temporal or extra-temporal epilepsy (Supplementary Figs. 8B and 12B). Patients with multi-focal epilepsy are often more difficult to treat because the seizures can originate from more than one brain area. This was reflected in our data where only one multi-focal patient had a successful surgical outcome and in turn, the predicted success probability of the source-sink model (Supplementary Figs. 8C) was commonly lower for these patients. Nevertheless, we saw no difference in clinical correspondence scores (Supplementary Fig. 12C).

We further analyzed the success probability and clinical correspondence with respect to treatment method (Supplementary Figs. 8D and 12D). Generally, patients who are surgical candidates (i.e., the seizure focus can be localized) undergo either resective surgery or laser ablation. In patients with poorly localizable or multiple seizure foci, or when the EZ is located in eloquent cortex, surgical resection may not be an option. In these cases, many patients opt for RNS treatment instead. Because of the higher clinical case complexity, patients who receive RNS treatment are not expected to achieve complete seizure freedom, but rather a reduction in seizure frequency.[12–14] This was reflected in the predicted probability of success by the source-sink model, which was overall lower for RNS patients compared to patients that received surgical treatment. In contrast, there was no observable correlation between p_s and surgical resection or laser ablation.

Finally, Supplementary Figs. 9 and 11 show the distributions of p_s and clinical correspondence scores, respectively, grouped by clinical centers. As both figures show, the distributions are similar across all centers, indicating that i) the tool generalized well across different datasets and ii) the overall probabilities and scores were not biased by any particular center
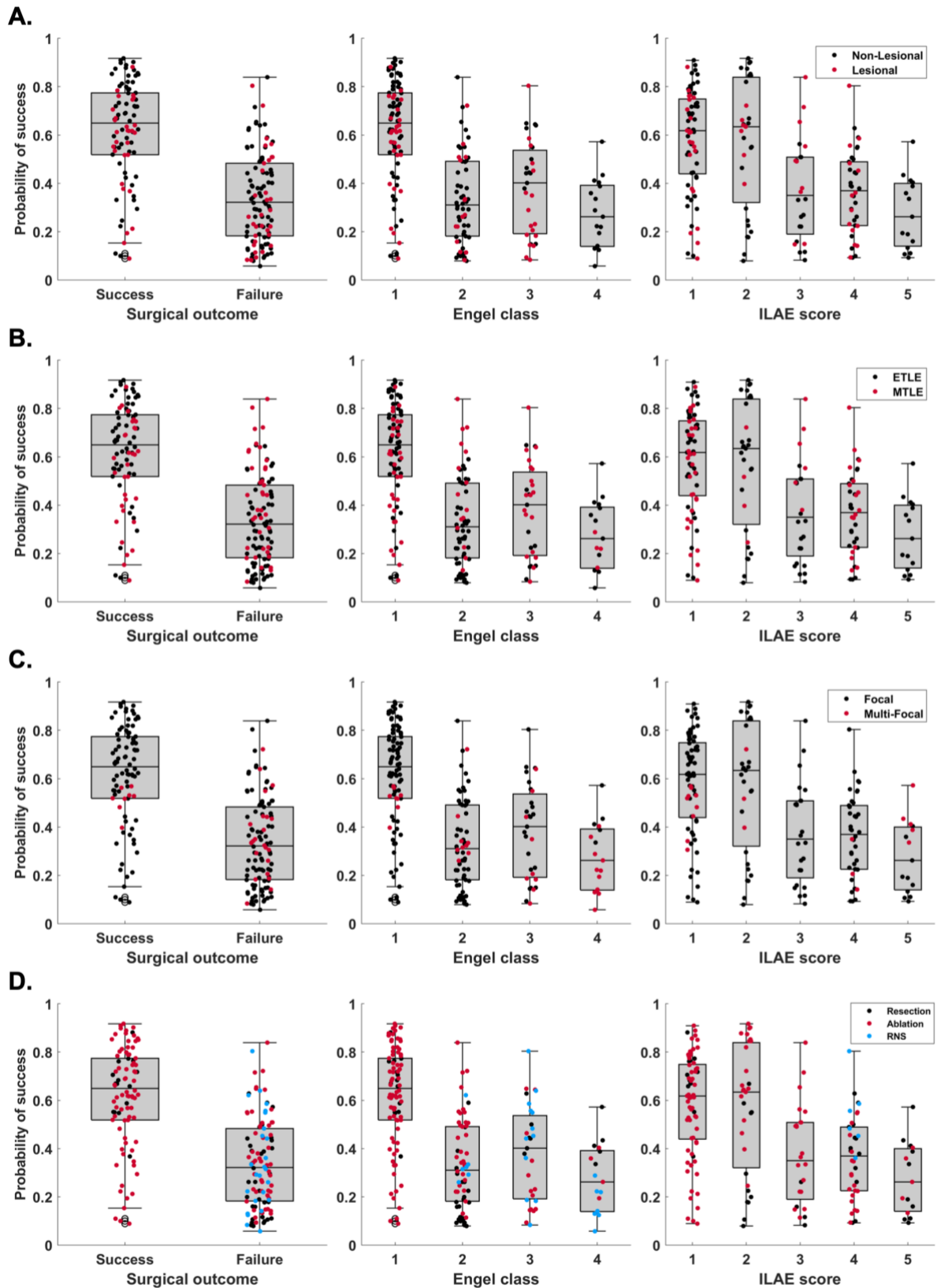
Supplementary Figure 8. Distributions of p_s across all CV folds as predicted by the source-sink model. The dots represent patients and are color-coded by different clinical covariates. A. Although lesional patients generally have a higher chance of a successful outcome, there is no correlation between p_s and whether patients have a lesion or not. B. Similarly, mesial-temporal epilepsy (MTLE) patients have higher success rates compared to extra-temporal epilepsy (ETLE) patients, but we see no correlation with p_s values. C. The tool is also agnostic to whether seizures start in one (focal) or a few (multi-focal) regions. D. Predicted success probability values corresponding to each treatment method are evenly distributed within each outcome category, suggesting that the tool is agnostic to treatment method. We note that for some cases, the source-sink algorithm may be in agreement with the CA-EZ, even though the patient did not become seizure free (e.g., if the EZ is in eloquent cortex and cannot be surgically removed). In those cases, the algorithm would accurately predict a higher success probability *if* the area was removed. However, since eloquent EZ is not removed, patients like these commonly receive RNS palliatively and are generally not expected to achieve complete seizure freedom. As such, RNS patients may have had a failed outcome even when an accurate SSM localization results in a higher predicted probability of success.
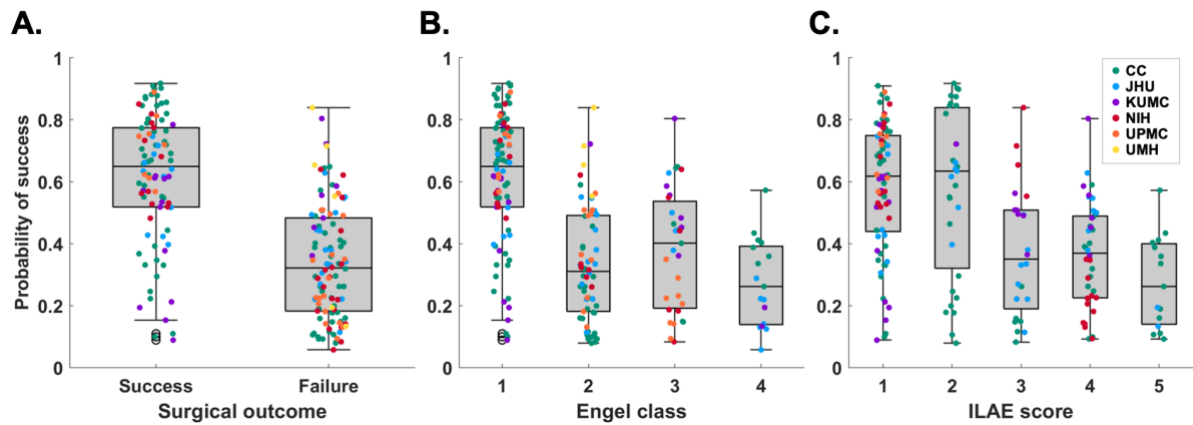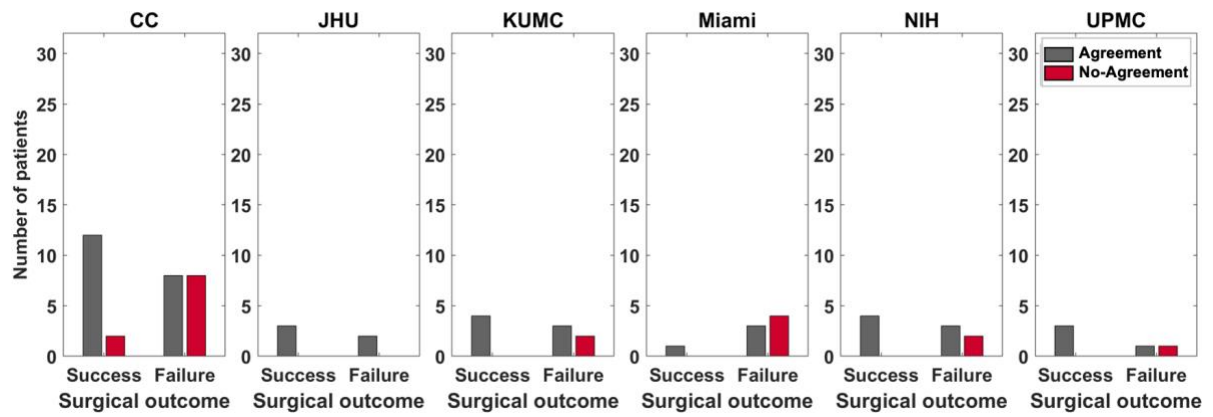
Supplementary Figure 9. Distributions of p_s across all CV folds as predicted by the source-sink model. The dots represent patients and are color-coded by different clinical centers. The tool generalizes well across data from different clinical centers indicated by the even distribution of p_s values across all centers.
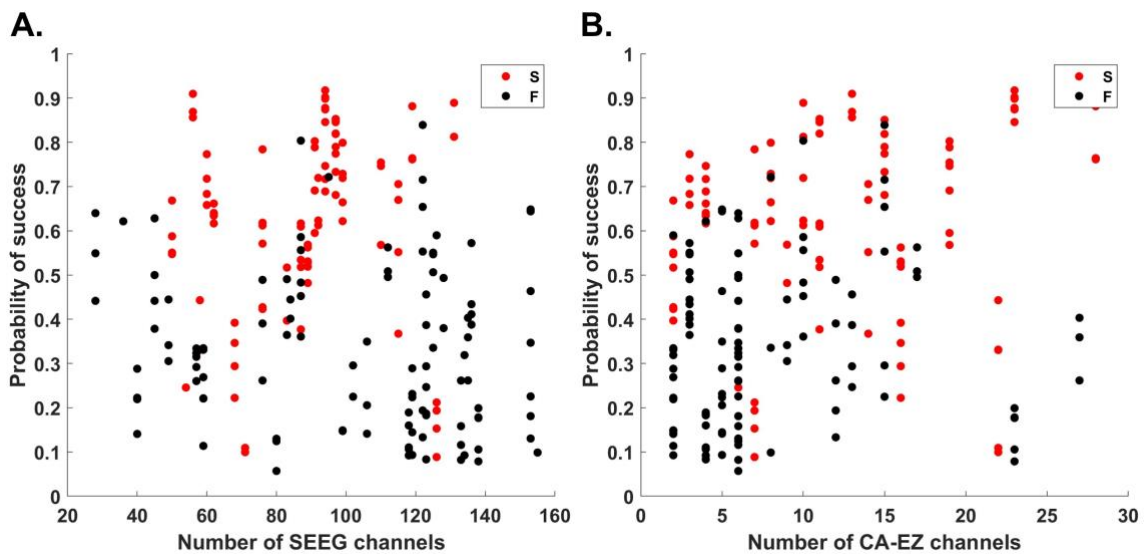

Supplementary Figure 10. Predicted probability of success (p_s) across all CV folds versus the number of implanted SEEG channels (A) and the number of clinically annotated EZ channels (B). The dots represent patients and are color-coded by surgical outcome. S = Success, F = Failure. There is no correlation between the number of channels and model predictions.

16

Supplementary Figure 11. Clinical correspondence stratified by clinical centers. The distribution of agreement scores is similar across centers.
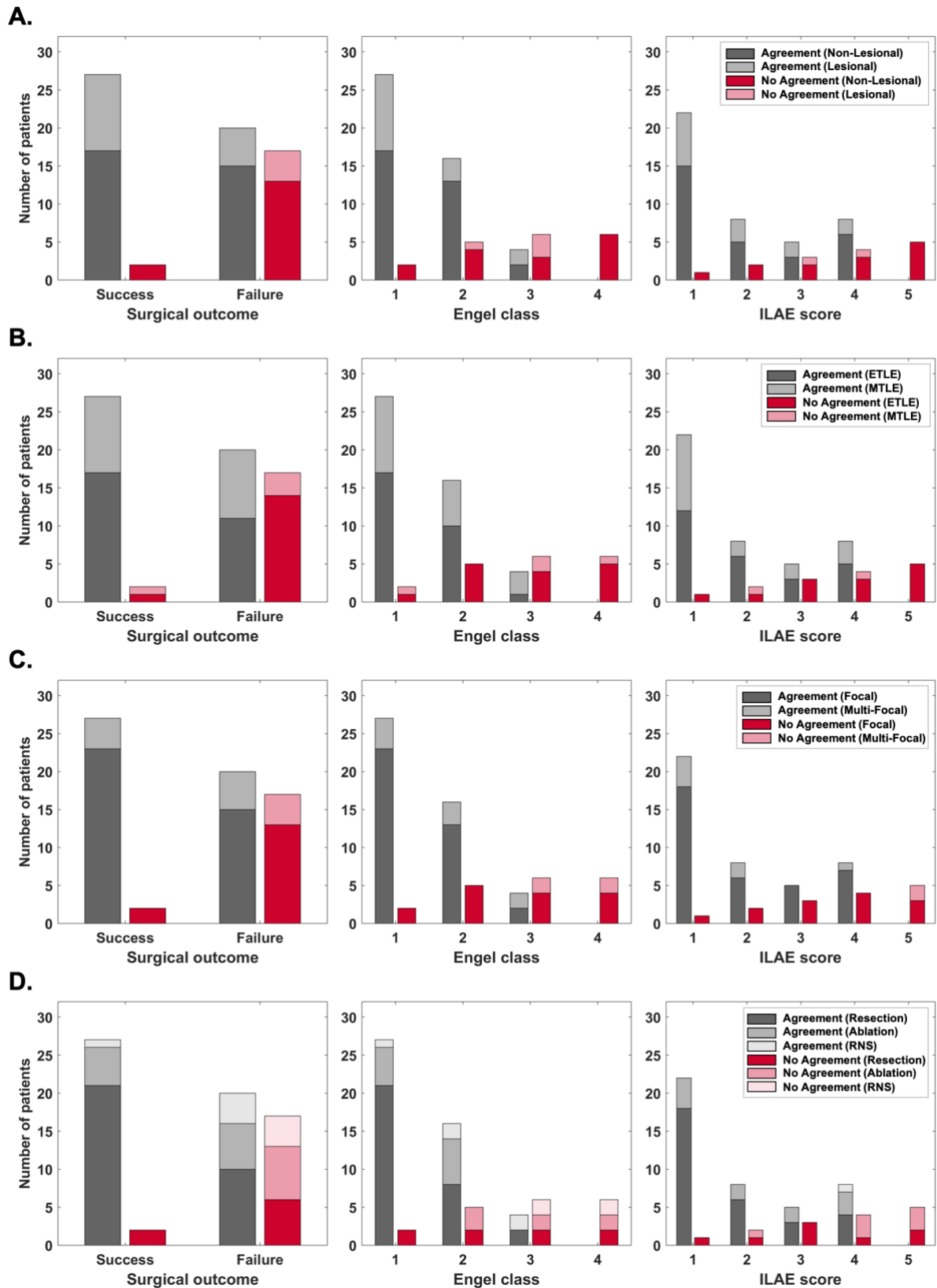
Supplementary Figure 12. Clinical correspondence stratified by clinical covariates. **A**. Lesional versus non-lesional patients. The proportion of each group is similar across all scores, indicating that the tool is not sensitive to whether patients have a visible lesion on MRI (which often leads to a higher chance of surgical success). **B**. Mesial-temporal lobe epilepsy (MTLE) versus extra-temporal lobe epilepsy (ETLE). The proportion of each group is similar across all correspondence scores. **C**. Epilepsy type defined as either focal or multi-focal. The tool is not sensitive to epilepsy type. **D**. The tool is agnostic to treatment methods. Note however, that in this dataset all but one RNS patients are classified as failed outcomes. RNS treatment is often used if the EZ is in eloquent cortex and as such, patients are not expected to achieve complete seizure freedom.

2.4 Quantifying CA-EZ and SSM correspondence

2.4.1 Results of EZ prediction using the source-sink metrics

Supplementary Fig. 13A shows the ROC curve obtained from training the SSI model and Supplementary Fig. 13B shows the test-set ROC curve for comparison. The AUC of the test set was 0.77 ± 0.01 which was highly comparable to the AUC of the training set, suggesting that the model generalizes well across different datasets.

Supplementary Fig. 14 shows resulting p_{EZ} distributions across all CV-folds. We note that since the EZ is a theoretical concept that cannot be directly measured, no ground truth of the true EZ exists and consequently, the boundaries of the exact EZ may be blur. Thus, channels labeled as EZ by the clinicians, may not always be as epileptic as their neighboring channels, and similarly, channels labeled as non-EZ may be in close proximity to the EZ and thus
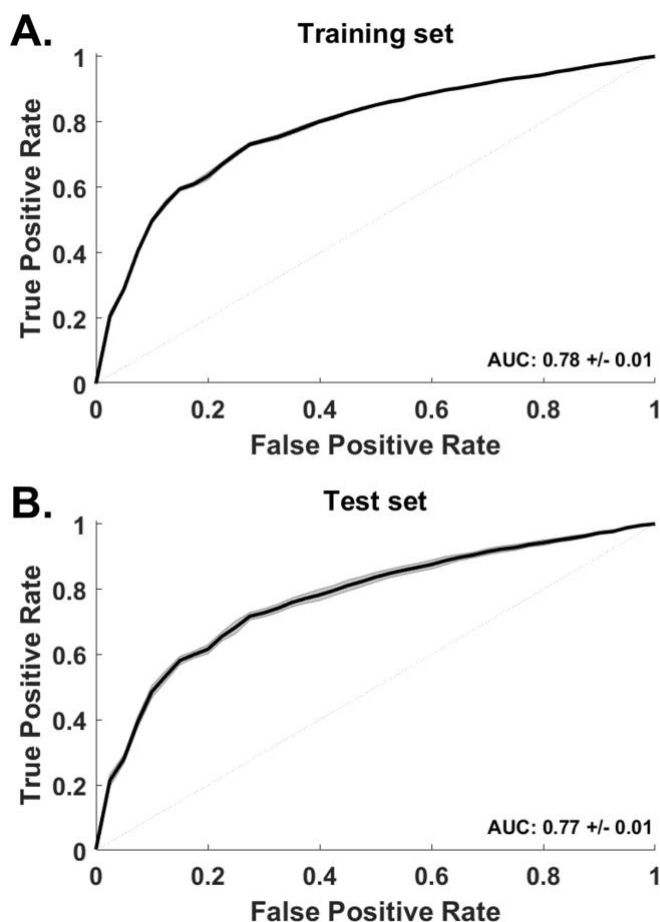

Supplementary Figure 13. ROC curves of the source-sink model across all CV-folds. A. Training set ROC curves. Black line shows the mean ROC across the ten CV folds and the shaded gray area represents one standard deviation. B. Test set ROC curves. The mean AUC of the test set is not significantly different from the AUC of the training set.
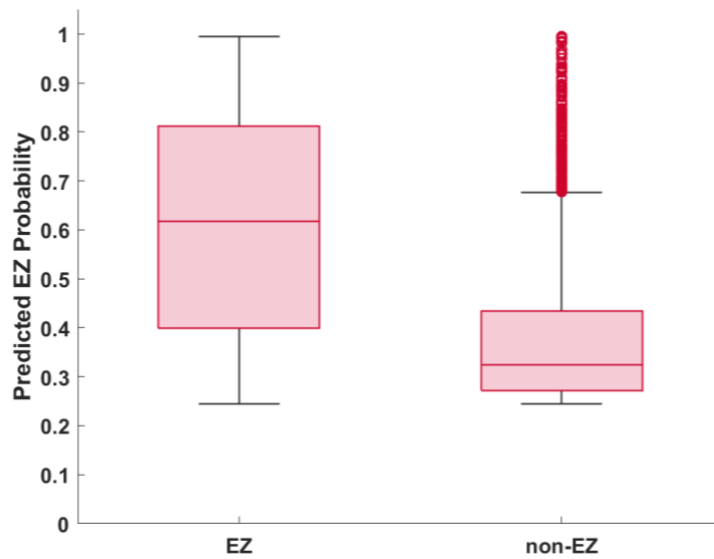
Supplementary Figure 14. Predicted EZ probability by the SSI model across all ten CV folds. Due to the high number of channels across the entire dataset, individual data points are not shown for better visualization purposes. There is a good separation of the distributions for EZ channels versus non-EZ channels. A large proportion of non-EZ outlier channels (red circles) belong to early spread regions or are located very close to the clinically annotated EZ regions.

demonstrate some level of epileptogenic behavior even if they were not removed. In fact, we found that a large proportion of the non-EZ outliers with the highest p_{EZ} values in our analyses belonged to early spread regions or were located very close to the clinically annotated EZ.

A decision threshold of $\alpha = 0.43$ was applied to the estimated probabilities (p_{EZ}) to predict each channel's epileptogenicity, rendering a test set accuracy of $72.5 \pm 1.2\%$ and an accuracy of $73.3 \pm 0.5\%$ on the training set (Supplementary Fig. 15). Further, the model yielded a test set precision of $0.73 \pm 0.02\%$, a sensitivity of 0.72 ± 0.02 and a specificity of 0.73 ± 0.01. As Supplementary Fig. 15 shows, the performance on the test set was highly comparable to that of the training set.
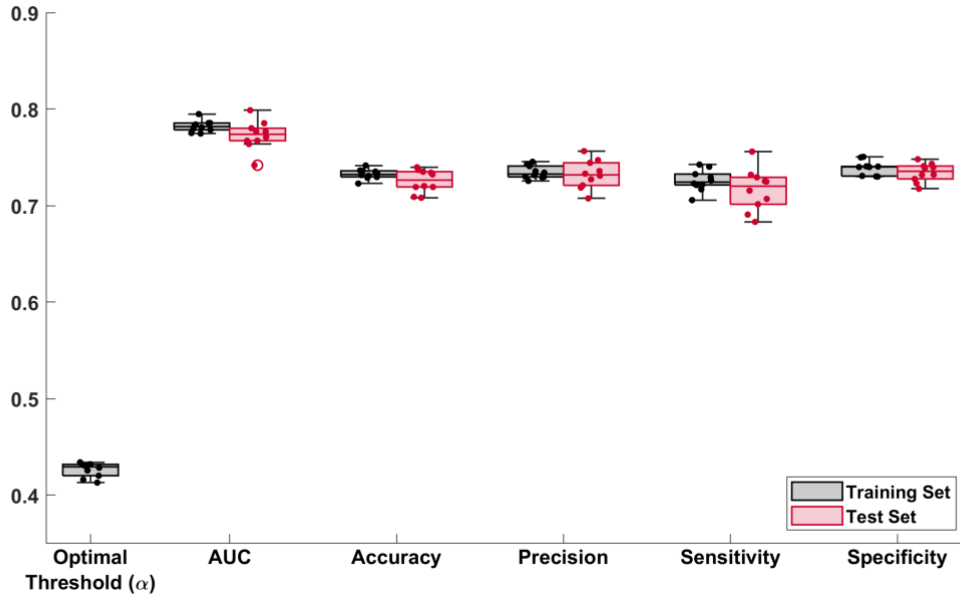
Supplementary Figure 15. Model performance of the training set (gray) and test set (red). Boxes show distributions of each metric across the ten CV folds and data points are represented with solid dots. Although there is more variability across the CV folds for the test set, the test set performance is comparable to that of the training set which suggests robustness of performance on different datasets.

2.5 CA-EZ regions are sinks at rest but become sources during seizures in success patients

In addition to computing the source-sink metrics across interictal recordings, we also investigated source-sink properties of the iEEG network during ictal periods. We did not receive ictal snapshots from all centers, so only a subset of the patient population ($n = 29$) was included in this part of the analysis. Supplementary Fig. 16 demonstrates the source-sink characteristics of the iEEG network as the brain moves from interictal towards a seizure in one success (left) and one failure (right) patient. For each patient, we computed each iEEG channel's SSI in 500-msec windows of one interictal and one ictal recording. Note that the two snapshots are not consecutive in time as the interictal snapshot is typically recorded hours before the seizure event. As Supplementary Fig. 16A shows, the CA-EZ channels have a high source-sink index (defined for each channel i as $SSI_i = sink_i * infl_i * conn_i$) in the success patient during interictal periods, suggesting they are top sinks strongly influenced by top sources. However, during and right after seizure, the same channels have a low SSI, that is, they are exhibiting a strong source-like behavior, which is in line with the source-sink
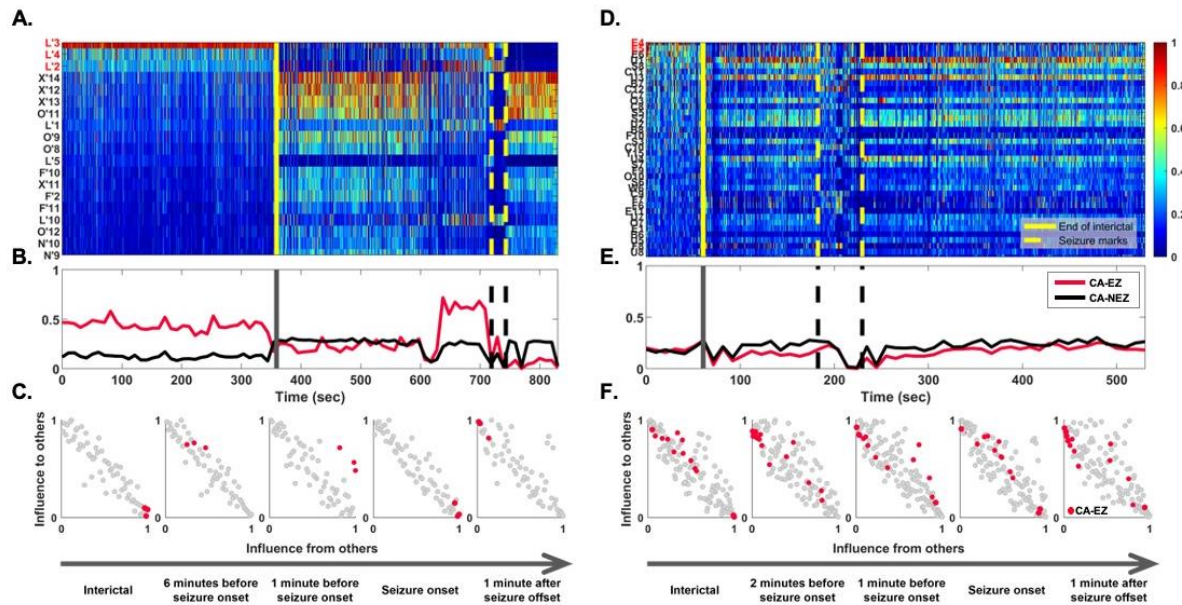
Supplementary Figure 16. Source-sink characteristics as the brain moves from resting state towards a seizure. Two patient examples. A. Source-sink index (SSI) of every channel during interictal (left) and ictal (right) periods, separated by the solid yellow line. Channels are arranged from highest to lowest average interictal SSI. CA-EZ channels are colored red. Only the top 30% of channels are shown for better visualization purposes, and all channels not shown have low SSI values. B. Average SSI of four CA-EZ versus CA-NEZ channels. In this success patient the CA-EZ channels have a much higher SSI compared to CA-NEZ channels during the interictal period. The SSI of CA-EZ channels drops significantly during seizure, as these channels become sources to initiate and spread seizure activity. D. Source-sink index of every channel over time. Only 2 out of 13 CA-EZ channels have a high source-sink index in this failure patient. E. Average source-sink index of the two groups. In this failure patient CA-EZ cannot be distinguished from CA-NEZ. E. Movement of CA-EZ channels in the 2D source-sink space over time. CA-EZ channels are top sinks during the interictal period (left), but move towards sources as the brain progresses towards a seizure. F. In this failure patient, there is little movement of CA-EZ channels as the brain moves from interictal to ictal state.

hypothesis. In contrast, only a small subset of CA-EZ channels (2 out of 13) are amongst the top sinks in the patient with a failed surgical outcome (Supplementary Fig. 16D) and there is little modulation of the SSI of these channels.

The temporal SSI modulation is summarized in Supplementary Fig. 16B and E. We computed the average source-sink index for two groups of interest: i) CA-EZ channels, and ii) all other channels not labeled as CA-EZ (CA-NEZ). Each curve was obtained by computing the average source-sink index of each channel group, in each window. The curves were smoothed by computing the index across 10-second windows instead of 500 msec. As Supplementary Fig. 16B shows, the CA-EZ channels have a much higher SSI compared to the rest of the network during the interictal period. However, this does not hold true for the failure patient (Supplementary Fig. 16E), where the mean index of the CA-EZ is not separable, or even slightly lower than the mean index of the CA-NEZ channels.

22

Supplementary Fig. 16C and F show an example of the 2D SS-space for the success and failure patients, respectively, computed in 10-second windows at different points in time relative to seizure onset. Despite the temporal stability of the SSMs across interictal recordings, the source-sink properties of the iEEG network modulate around seizure events. In success patients (Supplementary Fig. 16C) we frequently observed a movement of CA-EZ towards top sources as the brain progresses towards a seizure. Right before and at the onset of seizure however, the CA-EZ channels become sinks for a short period, perhaps as the rest of the network makes one last attempt to prevent the seizure from starting. During and right after seizure, the CA-EZ channels are again exhibiting a strong source-like behavior. The same cannot be said about the CA-EZ channels in failure patients (Supplementary Fig. 16F), where there was little movement of these channels in the SS-map over time.

Finally, Supplementary Fig. 17 compares the temporal SSI modulation in success versus failure patients. In the success patients, (Supplementary Fig. 17, top) the CA-EZ have a significantly higher SSI compared to the rest of the channels in the network in all windows except after the end of seizure ($p_a = 0.0132, p_b = 0.0029, p_c = 0.0015, p_d = 0.4240$). In contrast, the CA-EZ channels are not separable from the CA-NEZ channels at any time point ($p_{a,b,c,d} \gg 0.05$) in failure patients.
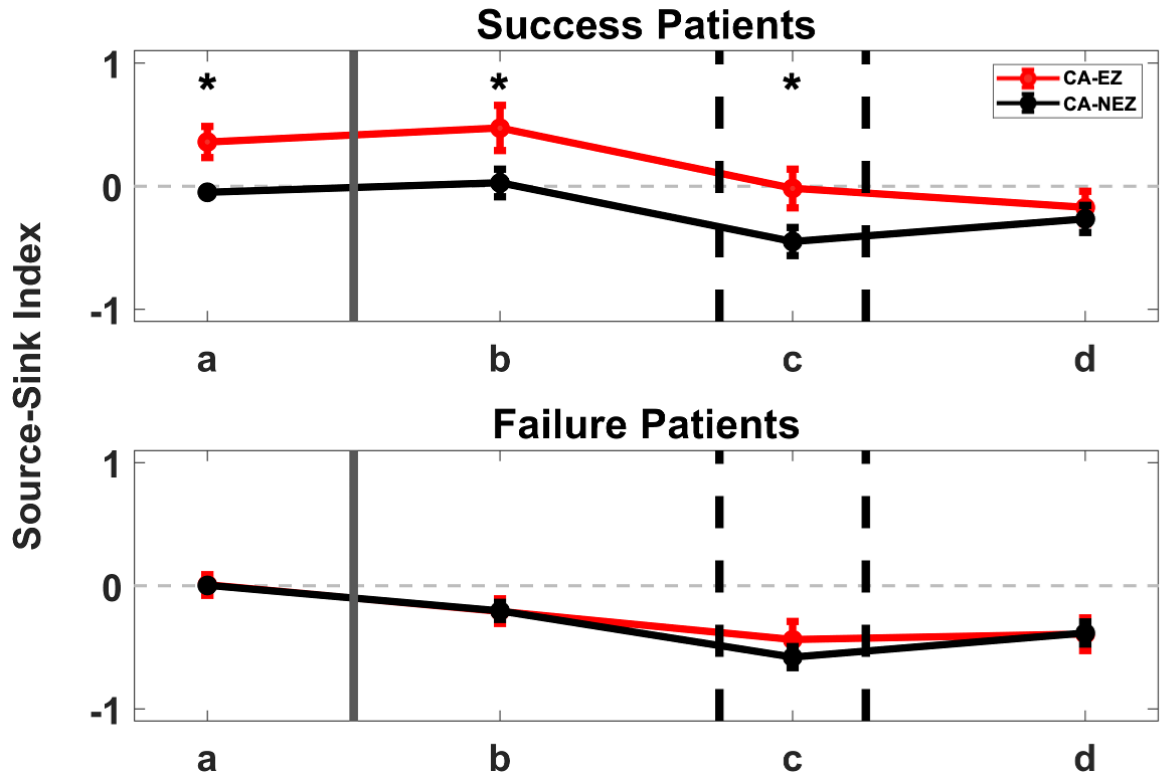
Supplementary Figure 17. Temporal SSI modulation in CA-EZ versus CA-NEZ channels. For each patient, SSI was computed in four predefined windows: a = 30 second window of the interictal recording, b = 60-30 seconds before the seizure event, c = during the seizure event, and d = 60-90 seconds after the end of seizure. Values were averaged over all CA-EZ and all CA-NEZ for each patient. For each set of channels, indices were normalized to the average SSI of the entire network at rest (window a). Each curve shows the mean $\pm$ standard error across 14 success patients (top) and 15 failure patients (bottom). CA-EZ channels have a higher SSI compared to CA-NEZ channels in success patients, but not in failure patients. The asterisks indicate a statistically significant difference between CA-EZ and CA-NEZ channels.

3 Supplementary References

1. Li A, Huynh C, Fitzgerald Z, et al. Neural fragility as an EEG marker of the seizure onset zone. *Nat Neurosci*. Published online August 5, 2021:1-10. doi:10.1038/s41593-021-00901-w

2. Perry R, Li A, Huynh C, et al. Manifold Oblique Random Forests: Towards Closing the Gap on Convolutional Deep Networks. *arXiv:190911799 [cs, stat]*. Published online August 7, 2021. Accessed October 19, 2021. http://arxiv.org/abs/1909.11799

3. Tomita TM, Browne J, Shen C, et al. Sparse Projection Oblique Randomer Forests. *arXiv:150603410 [cs, stat]*. Published online October 3, 2019. Accessed October 19, 2021. http://arxiv.org/abs/1506.03410

4. Crépon B, Navarro V, Hasboun D, et al. Mapping interictal oscillations greater than 200 Hz recorded with intracranial macroelectrodes in human epilepsy. *Brain*. 2010;133(1):33-45. doi:10.1093/brain/awp277

5. Staba RJ, Wilson CL, Bragin A, Fried I, Engel J. Quantitative analysis of high-frequency oscillations (80-500 Hz) recorded in human epileptic hippocampus and entorhinal cortex. *J Neurophysiol*. 2002;88(4):1743-1752. doi:10.1152/jn.2002.88.4.1743

6. Charupanit K, Lopour BA. A Simple Statistical Method for the Automatic Detection of Ripples in Human Intracranial EEG. *Brain Topography*. 2017;30(6):724-738. doi:10.1007/s10548-017-0579-6

7. Sindhu KR, Staba R, Lopour BA. Trends in the use of automated algorithms for the detection of high-frequency oscillations associated with human epilepsy. *Epilepsia*. 2020;61(8):1553-1569. doi:10.1111/epi.16622

8. Zelmann R, Mari F, Jacobs J, Zijlmans M, Dubeau F, Gotman J. A comparison between detectors of high frequency oscillations. *Clinical Neurophysiology*. 2012;123(1):106-116. doi:10.1016/j.clinph.2011.06.006

9. Navarrete M, Alvarado-Rojas C, Quyen MLV, Valderrama M. RIPPLELAB: A Comprehensive Application for the Detection, Analysis and Classification of High Frequency Oscillations in Electroencephalographic Signals. *PLOS ONE*. 2016;11(6):e0158276. doi:10.1371/journal.pone.0158276

10. Smith RJ, Hu DK, Shrey DW, Rajaraman R, Hussain SA, Lopour BA. Computational characteristics of interictal EEG as objective markers of epileptic spasms. *Epilepsy Research*. 2021;176(June):106704. doi:10.1016/j.eplepsyres.2021.106704

11. Smith RJ, Alipourjeddi E, Garner C, Maser AL, Shrey DW, Lopour BA. Infant functional networks are modulated by state of consciousness and circadian rhythm. *Network Neuroscience*. Published online 2021:1-17. doi:10.1162/netn_a_00194

12. Bergey GK, Morrell MJ, Mizrahi EM, et al. Long-term treatment with responsive brain stimulation in adults with refractory partial seizures. *Neurology*. 2015;84(8):810-817. doi:10.1212/WNL.0000000000001280

13. Skarpaas TL, Jarosiewicz B, Morrell MJ. Brain-responsive neurostimulation for epilepsy (RNS® System). *Epilepsy Research*. 2019;153:68-70. doi:10.1016/j.eplepsyres.2019.02.003

14. Hartshorn A, Jobst B. Responsive brain stimulation in epilepsy. *Ther Adv Chronic Dis*. 2018;9(7):135-142. doi:10.1177/2040622318774173